Superconducting Microsphere Magnetically Levitated in an Anharmonic Potential with Integrated Magnetic Readout

Citation for the original published paper (version of record):
Gutierrez Latorre, M., Higgins, G., Paradkar, A. et al (2023). Superconducting Microsphere
Magnetically Levitated in an Anharmonic Potential with Integrated
Magnetic Readout. Physical Review Applied, 19(5).
http://dx.doi.org/10.1103/PhysRevApplied.19.054047

PHYSICAL REVIEW APPLIED **19,** 054047 (2023)

Editors' Suggestion

Superconducting Microsphere Magnetically Levitated in an Anharmonic Potential with Integrated Magnetic Readout

Martí Gutierrez Latorre,[1] Gerard Higgins,[1,2] Achintya Paradkar,[1] Thilo Bauch,[1] and
Witlef Wieczorek[1,*]

[1] *Department of Microtechnology and Nanoscience (MC2), Chalmers University of Technology, Göteborg SE-412 96, Sweden*
[2] *Institute for Quantum Optics and Quantum Information (IQOQI), Austrian Academy of Sciences, Vienna, Austria*

(Received 26 October 2022; revised 23 March 2023; accepted 27 March 2023; published 12 May 2023;
corrected 21 June 2023 and 26 June 2023)

Magnetically levitated superconducting microparticles offer a promising path to quantum experiments with picogram to microgram objects. In this work, we levitate a 700 ng $\sim 10^{17}$ amu superconducting microsphere in a magnetic chip trap in which detection is integrated. We measure the center-of-mass motion of the particle using a dc superconducting quantum interference device magnetometer. The trap frequencies are continuously tunable between 30 and 160 Hz and the particle remains stably trapped over days in a dilution-refrigerator environment. We characterize the motional-amplitude-dependent frequency shifts, which arise from trap anharmonicities, namely, Duffing nonlinearities and mode couplings. We explain this nonlinear behavior using finite-element modeling of the chip-based trap potential. This work may constitute a first step toward quantum experiments and ultrasensitive inertial sensors with magnetically levitated superconducting microparticles.

DOI: 10.1103/PhysRevApplied.19.054047

I. INTRODUCTION

Systems of levitated nano- and microparticles in vacuum [1] offer extreme isolation of the particles from the environment as well as *in situ* tuning of the trapping potential [2,3]. These platforms provide novel opportunities for realizing ultrasensitive force [4–7] and acceleration sensors [8–12], for studying thermodynamics in the underdamped regime [13–15], for exploring many-body physics with massive objects [16–20] and for exploiting rotational degrees of freedom [21–24]. Recently, the center-of-mass (COM) motion of optically levitated nanospheres has been cooled to the motional ground state [25–29], opening up the possibility of performing quantum experiments with levitated nanoparticles [3,30,31]. There has also been tremendous progress in the field of electrically levitated nanoparticles toward reaching the quantum regime [22,32–35].

To extend quantum control from nano- to microparticles, magnetic levitation [36] has recently gained renewed interest [12,37–44]. Magnetic levitation can be used to levitate objects of different shapes [45,46] with masses ranging from picograms to tons [36]. It offers extreme isolation from the environment [38–40,43,47,48] and allows for tunable potential landscapes [49]. This combination of properties makes magnetically levitated particles particularly well suited for high-precision sensing of forces and accelerations [5,8–10,12,50], as well as for fundamental physics experiments with picogram to microgram objects [47–49]. Recent experimental developments in this direction include levitating micromagnets on top of superconductors [12,38,51–53], diamagnetic particles in strong magnetic fields [37,39–41,54], and superconducting microparticles in millimeter-scale superconducting magnetic traps [43,44,55].

We pursue magnetic levitation of superconductors in a superconducting magnetic trap, since this approach promises the least intrinsic mechanical dissipation [47,48]. Levitated superconductors in the Meissner state do not suffer from magnetic moment drift or intrinsic eddy current damping, unlike levitated magnets [5,12,38,52,53]. By using a persistent current magnetic trap [56], the trap can be made perfectly stable, unlike systems of diamagnetic particles levitated between strong magnets [39,54,57].

We levitate a superconducting microsphere in a fully chip-based system. The chip-based approach [44,58,59] enables higher magnetic field gradients and trapping frequencies, as well as the potential to scale up the system to levitate multiple particles on the same chip. We measure

---

[*] witlef.wieczorek@chalmers.se

the motion of the particle using magnetic pickup loops, which are coupled to a superconducting quantum interference device (SQUID) magnetometer. The pickup loops are integrated in the chip; this allows for precise positioning and enhanced measurement sensitivity. In future work, we will replace the SQUID by a flux-tunable superconducting microwave cavity [60–65] to achieve quantum control over the COM motion of the levitated microparticle [10,47–49].

In this work, we demonstrate stable levitation of a 48-μm-diameter (700-ng) superconducting microsphere over days. We smoothly tune the COM frequencies of the particle between 30 and 160 Hz by varying the trap current. We observe that the COM frequencies depend on the motional amplitudes. This arises from trap anharmonicities [32,66–70]. The observed behavior is consistent with estimations of the trap anharmonicities extracted from finite-element modeling (FEM) of our system. In future work, we will employ cryogenic vibration isolation [71,72] and feedback cooling [26,27,73] to reduce the motional amplitudes; the effects of trap anharmonicities will then be mitigated.

II. EXPERIMENTAL SETUP

The magnetic trap is produced by a current flowing in two superconducting coils, which are patterned on two silicon chips. The chips are stacked on top of each other to form an anti-Helmholtz-like configuration (see Fig. 1; for details, see Ref. [44]). The superconducting particle stably levitates near the minimum of the magnetic field of the trap. The particle is confined within a closed container given by the side walls of the hole in the top chip, the top surface of the bottom chip, and a glass slide on top of the hole. The force due to the magnetic trapping field is restoring within the bounds of the container, with a trap depth larger than 1×10^{10} K. To detect the particle motion, we use two pickup loops, which are integrated on the same chips (see Fig. 1).

As the particle moves, it changes the magnetic flux threading the pickup loops and thus the current induced in the loops. The pickup loops are connected to a commercial dc-SQUID magnetometer, which transduces the flux into a measurable voltage. Typical pickup efficiencies are $\{\eta_x, \eta_y, \eta_z\} = \{1.58, 3.3, 19.4\}$ mϕ_0 μm^{-1} for the three COM modes, in terms of the flux coupled into the SQUID and where ϕ_0 is the magnetic flux quantum. $\eta_z > \eta_x, \eta_y$ due to the geometry of the system (see Appendix B). The measurement noise floor (0.32 mϕ_0 Hz$^{-0.5}$) is limited by magnetic field fluctuations caused by trap-current fluctuations and corresponds to a noise floor of 200, 97, and 17 nm Hz$^{-0.5}$ for displacements along the x, y, and z directions, respectively. We connect the pickup loops in series to reduce the sensitivity to these field fluctuations. In future work, we will mitigate this noise by driving the trap using a persistent current [56], which should enable reaching the intrinsic noise floor of the SQUID (approximately 1 μϕ_0 Hz$^{-0.5}$).

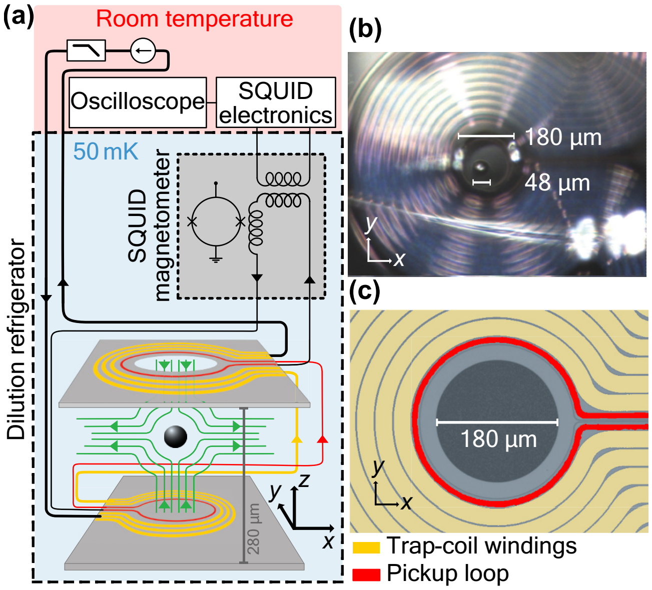

FIG. 1. The chip-based magnetic levitation setup. (a) A schematic of the experimental setup. The superconducting particle is levitated in a magnetic field minimum (magnetic field lines are shown in green). The magnetic trap coils and pickup loops are patterned on two stacked chips, which are housed in a dilution refrigerator. The vertical separation between the top and the bottom coils is 280 μm. Readout of the particle motion relies on coupling flux from the pickup loops into a SQUID magnetometer. (b) A microscope image of the two-chip trap. Through the 180-μm hole in the middle of the top chip, we see a 48-μm-diameter lead microsphere resting on the surface of the bottom chip. (c) A scanning electron microscope image of the top view of the two-chip trap, with false coloring.

The magnetic trap and the SQUID magnetometer are thermally connected to the mixing stage of a dilution refrigerator. This allows the experiment to operate between temperatures as low as 50 mK and as high as the critical temperature of the superconducting particle (6.2 K for lead). Before levitating, the particle thermalizes on the bottom chip surface to the temperature of the chip substrate [see Fig. 1(b)]. To lift the particle off the chip surface, we ramp the trap current up to 0.8 A to overcome the adhesive force between the particle and the chip surface. With a current of 0.8 A, the lift force is approximately 300 nN, which is usually sufficient to lift the particle. After that, the current is ramped down to the operating trap current.

III. CHARACTERIZATION OF CENTER-OF-MASS MOTION

Near the trap center, the particle experiences a harmonic trapping potential. The COM frequencies depend on the trap geometry, the density of the particle, and the trap current. The penetration depth (approximately 40 nm for lead) is much smaller than the particle radius (24 μm) and so the particle can be modeled as an ideal diamagnet with a magnetic susceptibility of -1 and its trapping frequencies ω_i are given by [74]

$$\omega_i = \nabla_i B \sqrt{\frac{3}{2\mu_0 \rho}} = \zeta_i \frac{\mu_0 N I}{R^2} \sqrt{\frac{3}{2\mu_0 \rho}}, \qquad (1)$$

where $\nabla_i B$ is the magnetic field gradient along the i direction at the trap center, μ_0 is the vacuum permeability, I is the trap current, N is the number of trap-coil windings, R is the trap-coil inner radius, ρ is the density of the particle, and ζ is a geometric factor. At the center of an ideal anti-Helmholtz configuration $2\zeta_x = 2\zeta_y = \zeta_z = 0.86$. In our system, $\zeta_x = 0.04$, $\zeta_y = 0.06$ and $\zeta_z = 0.12$ (our coils are separated by 280 μm and have inner radii of approximately 125 μm, as shown in Appendix B). The trap axes are indicated in Fig. 1(a).

Figure 2(a) shows the power spectrum of a levitated microsphere. Throughout this work, unless otherwise stated, we levitate a 48-μm-diameter lead sphere using a 0.5-A trap current and the cryostat temperature is 4 K. The peaks corresponding to the COM motion are colored. We identify these modes by comparing the peak frequencies with predictions from FEM simulations of our system [44,45]. We find good agreement between the measured and simulated COM frequencies. Peaks at the second harmonic of the COM frequencies are pronounced, particularly the second harmonic of the 40-Hz peak at 80 Hz. These peaks arise from the nonlinear pickup efficiency, rather than being due to actual particle motion at these frequencies. We describe these peaks further in Appendix C. In future work, we will feedback cool the particle, so that the effects of the nonlinear pickup will then be negligible.

The linear relation between the COM frequencies and the trap current given by Eq. (1) is shown in Fig. 2(b). We observe no significant difference between measuring this effect with a cryostat temperature of 50 mK or 4 K. We find good agreement between the measurement results and the FEM simulation results for the x and y modes. We attribute the 4% discrepancy for the z-mode frequency to simulation uncertainties in the FEM.

We confirm the inverse relation between the trapping frequency and the particle density of Eq. (1) by comparing the trapping frequencies of a lead particle and a tin-lead particle as we vary the trap current [see Fig. 2(c)]. The ratio of the frequencies is given by the square root of the ratio of the material densities.

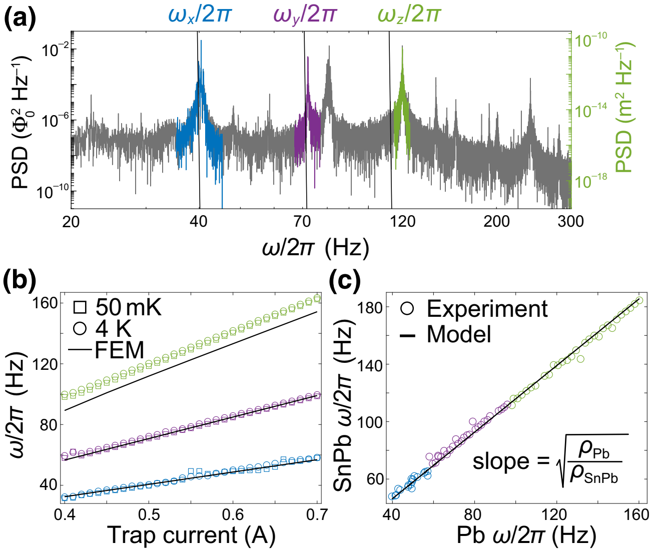

FIG. 2. The trap frequencies. (a) The power spectrum of the SQUID signal. The frequencies of the COM motion of the particle along the x, y, and z directions are highlighted. The black lines show the expected trap frequencies obtained from FEM simulations. The secondary y axis (green) shows the z amplitude in units of displacement. To obtain the x and y amplitudes in units of displacement, the secondary y axis has to be multiplied by 151 and 35, respectively. (b) The COM frequencies increase linearly with the trap current, as expected from Eq. (1). The results are similar when the cryostat temperature is at 50 mK and at 4 K. The lines show the simulated frequencies obtained from FEM. (c) When the same trap settings are used, a tin-lead sphere has a higher trap frequency than a lead sphere due to its lower density (see [Eq. (1)]).

We can stably levitate the superconducting sphere for days in the chip-based magnetic trap. Figure 3(a) shows the fluctuations of the COM frequencies of a levitated sphere over a 35-h measurement. We have yet to observe an upper limit to the levitation time, provided that the particle is not illuminated. When the particle is illuminated, as in Ref. [44], it heats up, loses superconductivity, and falls onto the bottom chip. When the particle is kept in the dark, as in this work, we have not yet observed any upper limit to the levitation time; we have measured up to 48 h.

Around once per day, we observe a sudden jump of all the COM frequencies of around 1 Hz (see Appendix E). We attribute these jumps to changes in the magnitude or orientation of trapped flux in the particle. Figure 3(a) shows 35 h of data in which we do not discern any such frequency jumps. The trapped flux will be the topic of a dedicated future investigation.

The COM motion of the particle does not thermalize at the cryostat temperature, since it is strongly driven by the vibrations of the cryostat. We estimate the mean amplitudes of the three modes to be 24, 10, and 7 μm for the x, y, and z modes, respectively, corresponding to an effective temperature of about 1×10^9 K. The energy in each mode ($m\omega_i^2\langle r_i^2\rangle$) fluctuates on a time scale of approximately 80 s, as shown by the autocorrelation functions in Fig. 3(b). The mode-energy fluctuations are due to the mode-amplitude fluctuations that occur over this time scale. By fitting the autocorrelation functions to exponential decay functions, we extract quality factors of 3400, 4500, and 9300 for the

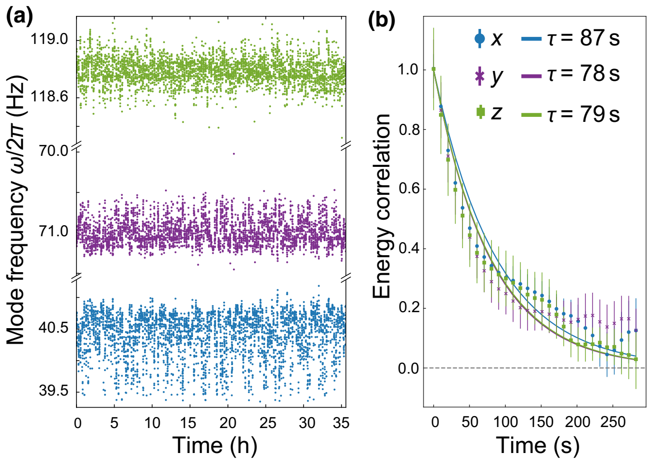

FIG. 3. The trap stability. (a) The particle levitates stably over 35 h and its COM-mode frequencies do not drift over that time. We explain the fluctuations of the frequencies by fluctuations of the COM-mode amplitudes together with frequency pulling. (b) The correlations of the COM-mode energies decay over around 80 s, because of fluctuations of the mode amplitudes over this time scale. The lines represent exponential fits.

x, y, and z modes, respectively [39]. We expect the quality factors to be limited by eddy current damping caused by normal-conducting metals in the vicinity of the levitated particle. In future work, we will mitigate this damping mechanism by surrounding the particle with a superconducting shield, with no normal-conducting metal within the shield.

IV. FREQUENCY PULLING

We can explain the COM-frequency fluctuations of Fig. 3(a) as resulting from the fluctuating mode amplitudes [Fig. 3(b)] together with frequency pulling, which describes the dependence of the COM frequencies on the mode amplitudes. It arises from quartic terms in the trapping potential of the form

$$U_{\text{pull}} = \sum_i \sum_j m\gamma_{ij} r_i^2 r_j^2, \tag{2}$$

which cause the motional frequencies to be shifted depending on the motional amplitudes according to [75]

$$\Delta\omega_i = \frac{3\gamma_{ii}}{\omega_i}\langle r_i^2\rangle + \sum_{j\neq i} \frac{2\gamma_{ij}}{\omega_i}\langle r_j^2\rangle. \tag{3}$$

The γ_{ii} terms in the potential are called Duffing nonlinearities, while the γ_{ij} terms describe couplings between the modes.

Experimental data showing frequency pulling are shown in Fig. 4. The spectral peak corresponding to the x mode (y mode) shifts depending on the amplitude of the x-mode motion in Fig. 4(a) [Fig. 4(b)]. This is described by Eq. (3). The remaining seven graphs showing the dependence of ω_i on $\langle r_j^2\rangle$ are included in Appendix D.

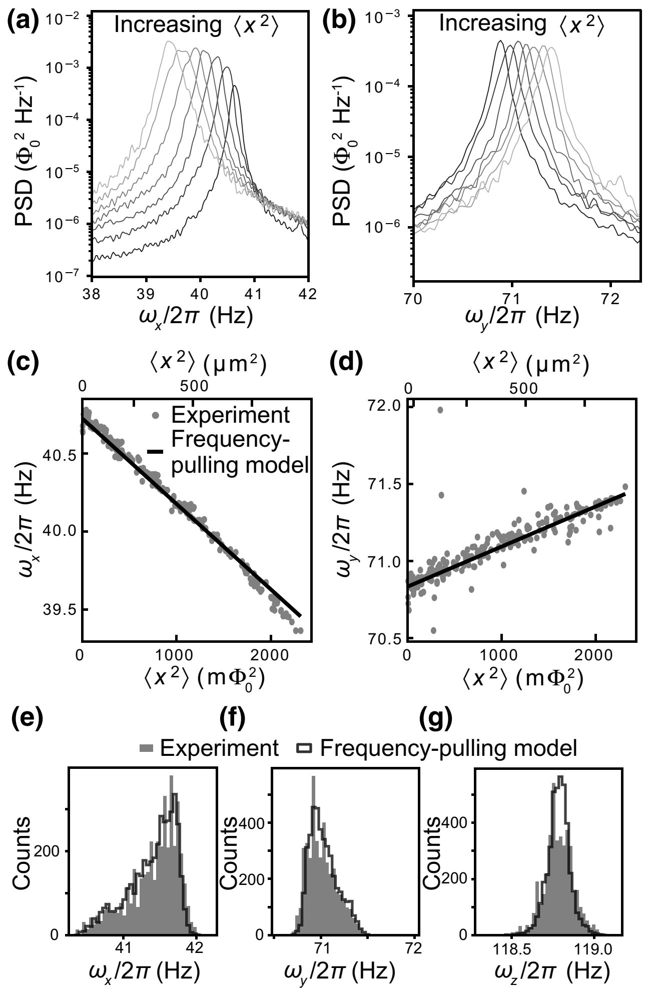

FIG. 4. Frequency pulling. The frequencies of (a) the x mode and (b) the y mode depend on the amplitude of the x mode; spectra represented in lighter colors have higher x-mode amplitudes. The (c) x- and (d) y-mode frequencies change linearly with the mean-square amplitude of the x mode. The slope of each model line is given by estimation of the trap anharmonicity obtained from FEM and by the estimated pickup efficiency η_x. (e)–(g) The fluctuating mode frequencies of Fig. 3(a) are described by asymmetric distributions. These distributions are reproduced well by using the same frequency-pulling model as in (c) and (d), together with the distribution of mode amplitudes from the experimental data.

The linear relation between the mode frequencies and the mean-square displacements [Eq. (3)] are shown in Figs. 4(c) and 4(d), in which the spectral peak frequencies ω_x and ω_y are plotted against the spectral peak area corresponding to the x mode (the remaining graphs of the same form are included in Appendix D). The slopes of these lines depend on the values of γ_{xx} and γ_{yx} as well as the pickup efficiency η_x. We extract estimates of γ_{ij} from

FEM simulations of our system (see Appendix A); this allows us to use the nine gradients (i.e., the nine linear relations between ω_i and $\langle x_j^2 \rangle$, for $i \in \{x, y, z\}$ and $j \in \{x, y, z\}$) to estimate the three efficiencies η_i (the values are quoted earlier). The estimated efficiencies are used to convert the lower x axes of Figs. 4(c) and 4(d) into the upper x axes and yield the secondary y axis of Fig. 2(a).

The estimation of the three efficiencies is an overconstrained problem, it yields fairly consistent results for the nine graphs. For instance, the estimation of η_x together with the FEM estimations of γ_{xx} and γ_{yx} describes the slopes in both Figs. 4(c) and 4(d) well.

To observe the frequency-pulling effect presented in Fig. 4 we do not control the motional amplitudes of the particle; instead, we filter a long 35-h data set in which the motional amplitudes fluctuate randomly. We separate the data into 10-s chunks and extract the mode frequencies and mode areas from each chunk.

To investigate the dependence of the mode frequencies on, e.g., the x-mode amplitude, we filter out the data in which the y- and z-mode amplitudes are high. Each point in Figs. 4(c) and 4(d) corresponds to one 10-s chunk. To produce the seven spectra in Figs. 4(a) and 4(b), we bin the power spectrum of each 10-s-long data set into seven bins, based on the x-peak areas and then we average the power spectra for each of the seven bins.

The mode-amplitude fluctuations together with frequency pulling describe the frequency fluctuations of Fig. 3(a). We represent the frequency distributions by histograms in Figs. 4(e)–4(g); we note that they are asymmetric. We also plot histograms based on the frequency-pulling model; the model histograms are constructed by predicting the mode frequencies for each 10-s interval of data based on the measured mode amplitudes, the nonlinear coefficients γ_{ij}, and the pickup efficiencies η_i. The model histograms describe the observed frequency fluctuations well.

Because the modes are coupled via the trap anharmonicity [Eq. (3)], we expect the average energies of the modes to be similar. We can estimate the mean energies of the modes $E_i \approx m\omega_i^2 \langle r_i^2 \rangle$ using the estimated pickup efficiencies η_i and we find that $E_x = 2.1E_y = 1.6E_z$. Because the estimated average energies rely on the estimated pickup efficiencies, the similarity of the average energies lends credence to our estimates of η_i.

V. CONCLUSIONS

In conclusion, we demonstrate an integrated superconducting chip device for magnetic levitation and detection of superconducting microparticles at millikelvin temperatures. We show a good understanding of the trap potential, the COM motion, and inductive coupling by comparing the trap models with measurements. Further, we demonstrate that the COM frequencies can be tuned via the trap current and that the system is stable over days. For the large motional amplitudes in our experiments, we observe nonlinear behavior and mode coupling of the COM particle motion, in the form of amplitude-dependent frequency shifts.

Future experiments will employ a cryogenic passive vibration isolation system [71,72], which will decouple the particle motion from external mechanical vibrations. Such vibration-isolation systems can attenuate our measured mechanical vibrations of about 1×10^{-8} m Hz$^{-0.5}$ by more than 6 orders of magnitude to achieve thermally driven COM motion at 50 mK. Further, the detection noise floor can be greatly reduced by the use of a persistent current trap [56] and improved magnetic shielding, which should allow us to reach the intrinsic noise floor of 1 $\mu\phi_0$ Hz$^{-0.5}$ of our commercial SQUID. Alternatively, the particle motion can also be measured using flux-sensitive superconducting microwave resonators [60–62,64,65]. Furthermore, the pickup efficiency can be increased by placing the pickup coil closer to the particle, by using multiwinding coils, and by improving the flux-transfer efficiency to the SQUID. We estimate that these measures will yield an improvement in the pickup efficiency of 4 orders of magnitude. This improvement is enabled by our understanding of the chip-based particle motion detection and the flexibility in the microfabrication of pickup loops of our chip-based approach. Overall, the reduction of technical noise and increase in pickup efficiency should enable feedback cooling to the quantum ground state [26,27,73] of the COM motion of microparticles, which would serve as a gateway to generating quantum states of nano- to microgram masses [10,47,48].

The supporting data for this article have been made available [76].

ACKNOWLEDGMENTS

We gratefully acknowledge Axel Eriksson, Andreas Isacsson, Philip Schmidt, Joachim Hofer, and Fabian Resare for insightful discussions and also Joachim Hofer for the sharing of code. This work was supported in part by the European Union Horizon Europe 2021–2027 framework program under Grant Agreement No. 101080143 (SuperMeQ), the QuantERA project C'MON-QSENS!, the Knut and Alice Wallenberg Foundation through a Wallenberg Academy Fellowship (W.W.), by the Wallenberg Center for Quantum Technology (WACQT, A.P.), by the Chalmers Excellence Initiative Nano, and by the Swedish Research Council (Grant No. 2020-00381, G.H.). Sample fabrication was performed in the Myfab Nanofabrication Laboratory at Chalmers. Simulations were performed on resources provided by the Swedish National Infrastructure for Computing (SNIC) at Tetralith, Linköping University, partially funded by the Swedish Research Council (Grant No. 2018-05973).

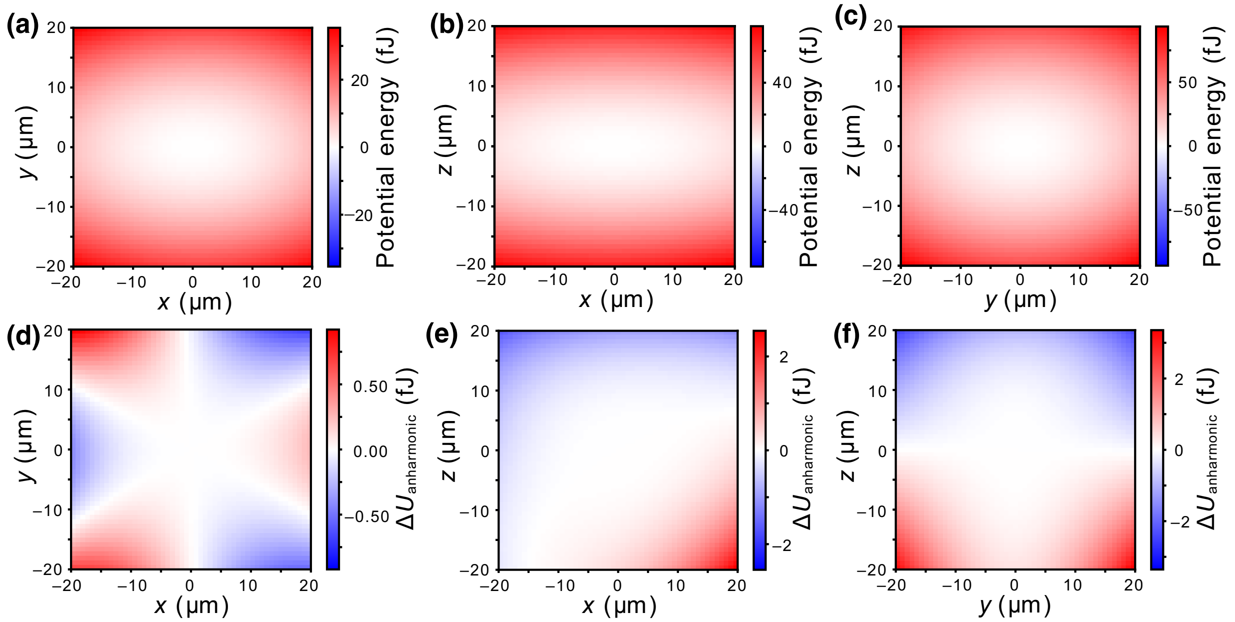

FIG. 5. The model of the potential-energy landscape of a 48-μm-diameter particle in the chip trap. The model coefficients are extracted from FEM. (a)–(c) Two-dimensional slices of the potential energy. (d)–(f) Contributions from the cubic and quartic terms to the potential landscape.

APPENDIX A: EXTRACTING THE TRAP ANHARMONICITY FROM FEM

We consider anharmonicities in the trapping potential up to quartic terms. The potential can then be described as

$$U = \sum_i \tfrac{1}{2} m\omega_i^2 r_i^2 + \sum_i\sum_j\sum_k m\beta_{ijk} r_i r_j r_k + \sum_i\sum_j\sum_k\sum_l m\gamma'_{ijkl} r_i r_j r_k r_l. \tag{A1}$$

The force acting on the particle is

$$F_i = -\frac{dU}{dr_i}. \tag{A2}$$

The FEM simulations give us the force acting on the particle due to the trapping potential at different displacements, as described in Ref. [45]. We fit the FEM results by using Eq. (A2), with the coefficients of the trapping potential of Eq. (A1) as free parameters. In this way, we extract the trapping potential coefficients from the FEM simulations.

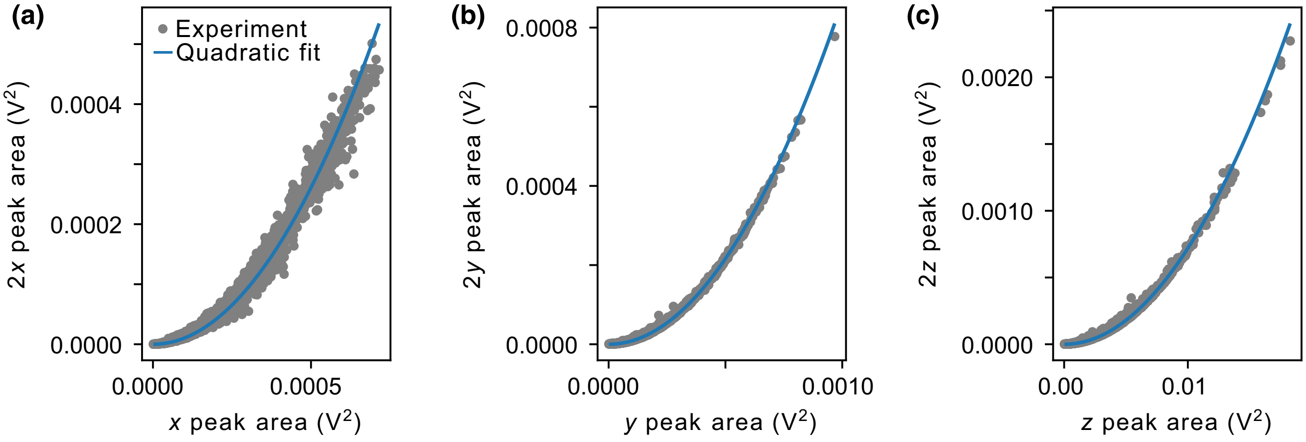

FIG. 6. A comparison of the fundamental- and second-harmonic-mode spectral areas. The areas of the spectral peaks at the second-harmonic frequencies increase quadratically with the areas of the spectral peaks at the fundamental frequencies.

Note that in comparing γ' with γ from the main text,

$$\begin{aligned}\gamma_{ii} &= \gamma'_{iiii},\\ \gamma_{ij} = \gamma_{ji} &= \tfrac{1}{3}\gamma'_{iijj} = \tfrac{1}{3}\gamma'_{ijji} = \tfrac{1}{3}\gamma'_{jjii}\\ &= \tfrac{1}{3}\gamma'_{ijij} = \tfrac{1}{3}\gamma'_{jiij} = \tfrac{1}{3}\gamma'_{jiji},\end{aligned} \tag{A3}$$

The potential energy that we calculate based on fitting the FEM simulations is represented in Fig. 5. We calculate the potential energy in three dimensions; in Fig. 2(d), slices are shown. Figure 5 also shows the relative contribution of the cubic and quartic terms to the potential.

APPENDIX B: MEASUREMENT OF PARTICLE MOTION

As the particle displacement oscillates, the magnetic flux threading the pickup loops oscillates in response. This oscillating flux of the pickup loops is transferred to the SQUID loop. The flux at the SQUID loop is converted into a voltage signal. In this appendix, each of these steps is described in turn.

1. Inductive coupling to particle motion

We estimate the response of the change of flux threading the pickup loops in response to the displacement of the particle along x, y, and z by treating the trapping field as a magnetic quadrupole field (which is a good approximation near the center), using Eq. (5) from Ref. [74] and using knowledge of the geometry of our system (represented in Fig. 7). The results are shown in Fig. 8. The response to displacement along all directions is nonlinear; that is, the response has strong quadratic components (-7.5, -6.0, and -3.7 mϕ_0 μm^{-2}), which we describe by the parameter u_i in Appendix C 2. We note that the response of the pickup to displacement along the z direction is largely linear, whereas the response to the x and y displacements has a clear quadratic component. The response can be made more linear along the x and y directions by changing the geometry such that the particle equilibrium position is displaced further from the center of the pickup loops. Because the pickup loops are connected in series, the overall pickup-loop flux is the sum of the fluxes in each loop.

2. Flux transfer from the pickup loops to the SQUID loop

Figure 9 shows how the pickup loops are electrically connected to the SQUID via an input coil. The flux transfer is given by

$$\begin{aligned}\phi_{\text{SQUID}} &= \frac{M_{\text{input}}}{\left(L_{\text{pickup}} + L_{\text{input}} + L_{\text{parasitic}}\right)}\phi_{\text{pickup}}\\ &= \eta_{\text{flux}} \times \phi_{\text{pickup}},\end{aligned} \tag{B1}$$

where $L_{\text{input}} \approx 24$ nH is the input coil inductance, $L_{\text{parasitic}} \approx 33$ nH is the parasitic inductance, which is dominated by the inductance of the twisted wire pairs, $L_{\text{pickup}} \approx 0.72$ nH is the pickup inductance, and $M_{\text{input}} \approx 0.87$ nH is the mutual inductance between the SQUID loop and the input-coil inductance. Using these values, we estimate the flux-transfer efficiency $\eta_{\text{flux}} = 3.1 \times 10^{-2}$. By improving the inductance matching, η_{flux} can be improved to 0.5.

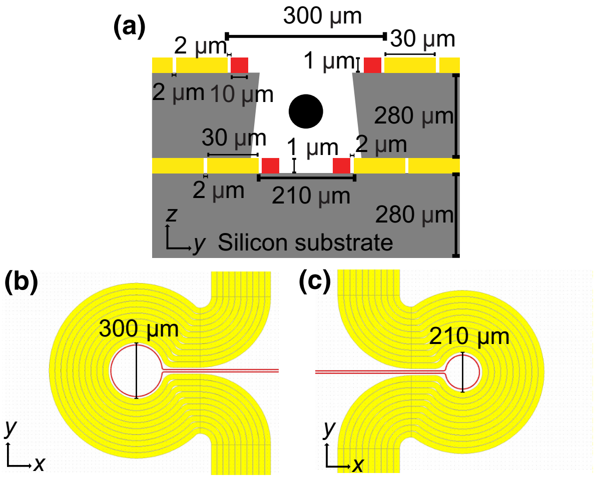

FIG. 7. The chip trap. (a) A schematic of the cross section of the stacked two-chip trap. The layout of the (b) top and (c) bottom coils. The inner radius of the bottom coil is reduced to achieve a stronger lift force on the particle.

Based on the dependence of the pickup-loop flux on the particle displacement (Fig. 8) and the flux-transfer efficiency from the pickup loops to the SQUID loop Eq. (B1), we make independent estimates of the pickup efficiency in the pickup loop $\eta^{\text{pickup}}_{i,\text{quad-field}} = 40$, 15.3, and 600 m$\phi_0$ μm^{-1}. These values are close to those found by using the measurement data and the model for the potential energy, where we obtain $\eta^{\text{pickup}}_{i,\text{model}} = 50$, 106, and 625 m$\phi_0$ μm^{-1}. We note that we obtain the latter values by dividing the pickup efficiencies in terms of flux in the SQUID, $\eta_i = 1.58$, 3.3, and 19.4 mϕ_0 μm^{-1}, by the flux-transfer efficiency η_{flux}, i.e., $\eta^{\text{pickup}}_{i,\text{model}} = \eta_i/\eta_{\text{flux}}$. The small discrepancy may arise because our estimates of the response of the pickup loops to displacements along x and y using the data in Fig. 8 depend critically on our knowledge of the equilibrium position of the particle, due to the nonlinearity of the pickup efficiency. Additionally, we make the simplifying assumption in Appendix B 1 of a magnetic quadrupole field at the trap center.

3. Flux in SQUID loop converted to SQUID voltage

We operate the SQUID in flux-locked loop mode. Then, the SQUID output voltage V_{out} is related to the SQUID

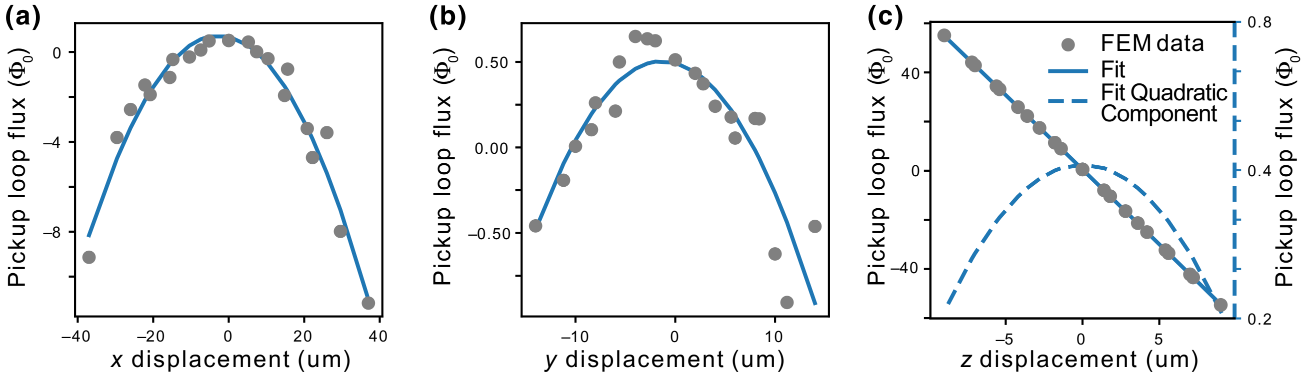

FIG. 8. The dependence of flux in the pickup loop on the particle displacement. The pickup-loop flux responds quadratically to the particle displacements along all directions. There are also linear components to the response. The response to displacement along the z direction is near linear. The nonlinear response of the pickup-loop flux leads to additional peaks in the spectrum of Fig. 10 and explains the behavior of Fig. 6.

loop flux ϕ_{SQUID} by

$$\phi_{\text{SQUID}} = \frac{M_{\text{Finput}}}{R_{\text{F}}} V_{\text{out}}^{\text{FLL}}, \tag{B2}$$

where $M_{\text{Finput}} = 38$ pH is the mutual inductance between the feedback electronics and the SQUID and $R_{\text{F}} = 10$ kΩ describes the resistor used in the feedback electronics.

APPENDIX C: HARMONICS IN SPECTRA

As well as observing the peaks in the spectra at frequencies ω_x, ω_y and ω_z corresponding to COM motion along the x, y, and z directions, we observe strong peaks at frequencies $2\omega_x$, $2\omega_y$ and $2\omega_z$ (see the power spectrum in Fig. 10).

We observe that the peak areas of the second-harmonic peaks grow quadratically with the peak areas of the respective fundamental peaks, as shown in Fig. 6. The fundamental and harmonic peak areas A_{fi} and A_{hi} are related by

$$A_{hi} = R_i^{\text{obs}} A_{fi}^2. \tag{C1}$$

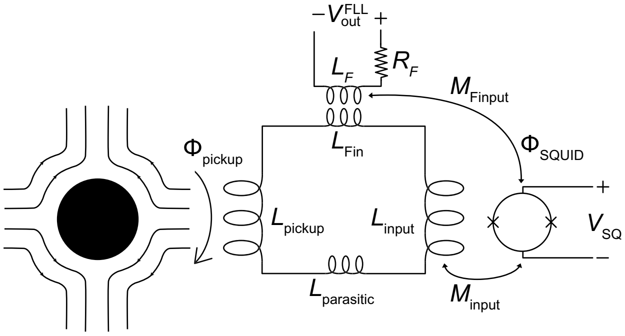

FIG. 9. A schematic circuit diagram of the single-stage dc-SQUID magnetometer used to detect the particle motion [77].

The factor R_i^{obs} describes the observed quadratic relation between the peak areas; it is different for each mode. From the data in Fig. 6, we extract $R^{\text{obs}} = 1000$, 870, and 7.2 V^{-2} for the x, y, and z modes, respectively (in this appendix, we work with the spectral peak areas in units of V^2, which is why R has units of V^{-2}).

The construction of Fig. 6 involves breaking the 35-h-long data set, which is used in Figs. 3 and 4 of the main text, into 10 s chunks. We then calculate the power spectrum for each 10-s chunk and extract the peak areas for the three fundamental and three second-harmonic peaks and compare them.

Below, we estimate that the actual motion of the particle at frequencies $2\omega_x$, $2\omega_y$ and $2\omega_z$ arising from the trap anharmonicity is negligible. Instead, we believe that

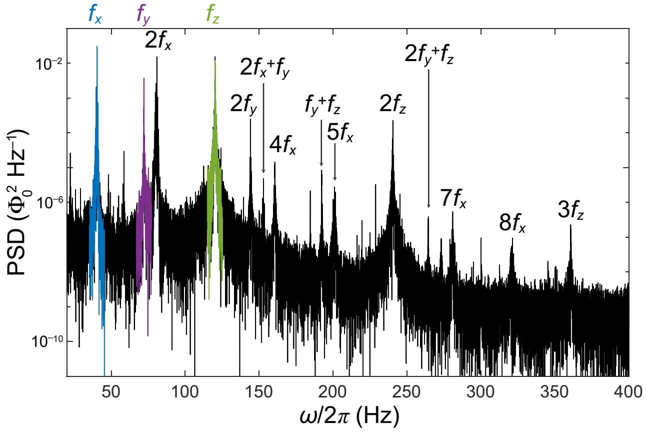

FIG. 10. The power spectrum displays peaks at the harmonics and at mixing frequencies, as well as peaks at the COM motional frequencies of the particle (the fundamental peaks are colored). The harmonics arise primarily from the nonlinearity of the pickup.

the second harmonics arise primarily due to the pickup nonlinearity.

1. Particle motion at the second-harmonic frequency arising from the trap anharmonicity

In a potential of the form

$$U = \tfrac{1}{2} m\omega_x^2 x^2 + \tfrac{1}{3} m\beta_{xxx} x^3, \tag{C2}$$

the particle will move with a component at frequency ω_x and a component at frequency $2\omega_x$. The amplitudes of these motions, at the fundamental frequency and at the harmonic frequency, are related by

$$\langle x_h^2 \rangle = \frac{\beta_{xxx}^2 \langle x_f^2 \rangle^2}{18\omega_x^4}, \tag{C3}$$

provided that the cubic term in the potential is a perturbation and provided that the motional amplitudes are small.

We derive this equation by solving the equation of motion in this potential looking for a solution of the form

$$x(t) = X_1 \sin \omega_x t + X_2 \sin (2\omega_x t + \theta) \tag{C4}$$

in the regime where $X_2 \ll X_1$.

Because the peak areas are related to the mean-square amplitudes by $\langle x_i^2 \rangle = \eta_i A_i$, we expect the nonlinearity of the trapping potential to give

$$R_i^{\text{trap}} = \frac{A_{hi}}{A_{fi}^2} = \frac{\beta_{iii}^2 \eta_i}{18\omega_i^4}. \tag{C5}$$

Thus, using the values β_{iii} extracted from FEM (see Appendix A), we expect $R^{\text{trap}} = \{6 \times 10^{-1}, 1.9 \times 10^{-4}, 2.1 \times 10^{-4}\}$ V^{-2} for the x, y, and z modes. These values are much smaller than the observed values R^{obs} and so the second-harmonic peaks do not arise from motion of the particle at the second-harmonic frequencies.

2. Second-harmonic peaks caused by the pickup nonlinearity

A particle in a one-dimensional harmonic potential moves according to

$$x(t) = X \sin \omega_x t. \tag{C6}$$

As described in Appendix B 1 and Fig. 8, the flux threading the pickup loops depends nonlinearly on the particle position $x(t)$. This can be captured by the quadratic function

$$\phi(t) = ux(t)^2 + vx(t) + w \tag{C7}$$

$$= \frac{uX^2}{2}(1 - \cos 2\omega t) + vX \sin \omega t + w. \tag{C8}$$

Here, v and u are conversion factors from particle displacement to pickup-loop flux; v describes the linear response of the pickup loop, while u describes the quadratic response. w is an offset.

The SQUID voltage signal is related to the flux threading the pickup loops by

$$V(t) = k\phi(t), \tag{C9}$$

where we define the conversion factor k, and so the voltage signal is related to the particle position by

$$V(t) = px(t)^2 + qx(t) + r \tag{C10}$$

$$= \frac{pX^2}{2}(1 - \cos 2\omega t) + qX \sin \omega t + r, \tag{C11}$$

where q and p are conversion factors from particle displacement to SQUID voltage; q describes the linear response of the SQUID, while p describes the quadratic response and r is an offset. We see that

$$\frac{p}{q} = \frac{u}{v}. \tag{C12}$$

In the power spectrum of the voltage signal, the area of the fundamental peak is A_f and the area of the harmonic peak is A_h, and so

$$A_h = \frac{p^2 X^4}{8} \tag{C13}$$

and

$$A_f = \frac{q^2 X^2}{2}. \tag{C14}$$

Earlier, we have defined

$$\eta A_f = \langle x^2 \rangle = \frac{X^2}{2}, \tag{C15}$$

so we identify

$$\eta = \frac{1}{q^2}. \tag{C16}$$

Overall, the nonlinearity of the pickup should give

$$R^{\text{PU}} = \frac{A_h}{A_f^2} = \frac{u^2 \eta}{2v^2}. \tag{C17}$$

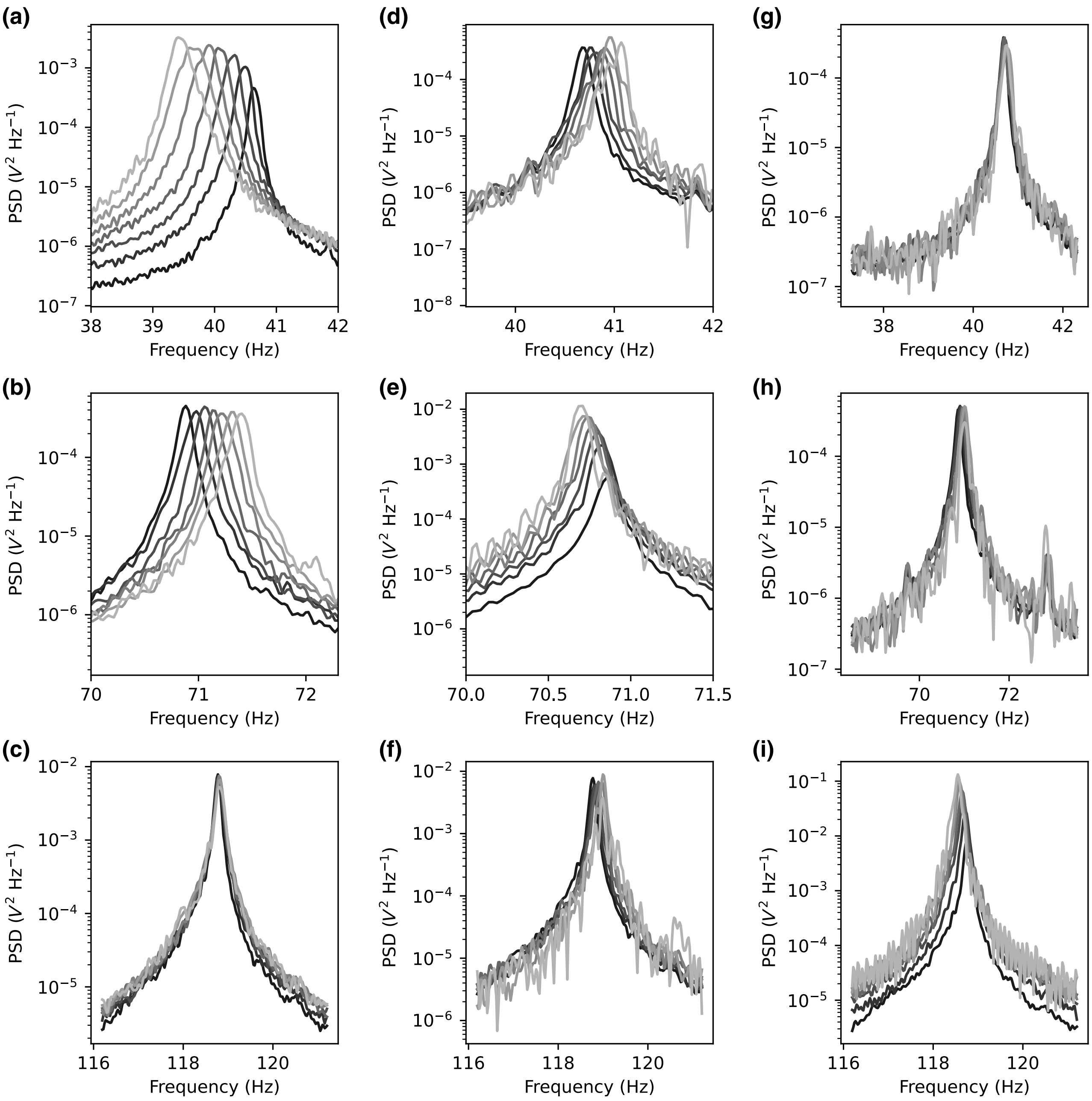

FIG. 11. Frequency pulling. The spectral peaks corresponding to the COM frequencies depend on the COM-mode amplitudes. In each panel, the lighter-colored spectra have higher mode amplitudes. (a)–(c) $\langle x^2 \rangle$ is different for different spectra (both $\langle y^2 \rangle$ and $\langle z^2 \rangle$ are relatively low). (d)–(f) Similarly, $\langle y^2 \rangle$ is different for different spectra (both $\langle x^2 \rangle$ and $\langle z^2 \rangle$ are relatively low). (g)–(i) Similarly again, $\langle z^2 \rangle$ is different for different spectra (both $\langle x^2 \rangle$ and $\langle y^2 \rangle$ are relatively low).

We extract u_i and v_i for the different directions x, y, and z using the data in Fig. 8 and we extract η from the comparison of the observed frequency pulling (see Appendix D) with the trap anharmonicities given by FEM (see Appendix A). Thus, we estimate $R^{\text{PU}} = \{2.5 \times 10^4, 2.3 \times 10^4, 1.6 \times 10^{-3}\}$ V^{-2}. These are order-of-magnitude estimations, since the estimations of v_i depend critically on our estimation of the position of the trap center. The estimates R^{PU} are similar in magnitude to the observed values of R^{obs} for the x and y modes and so we believe that the spectral peaks at the second harmonics arise from the nonlinear pickup.

APPENDIX D: FREQUENCY PULLING

Figures 11 and 12 employ the same data set and analysis method as is used to construct Figs. 4(a)–4(d) of the main text. While Figs. 4(a)–4(d) shows the dependence of ω_x

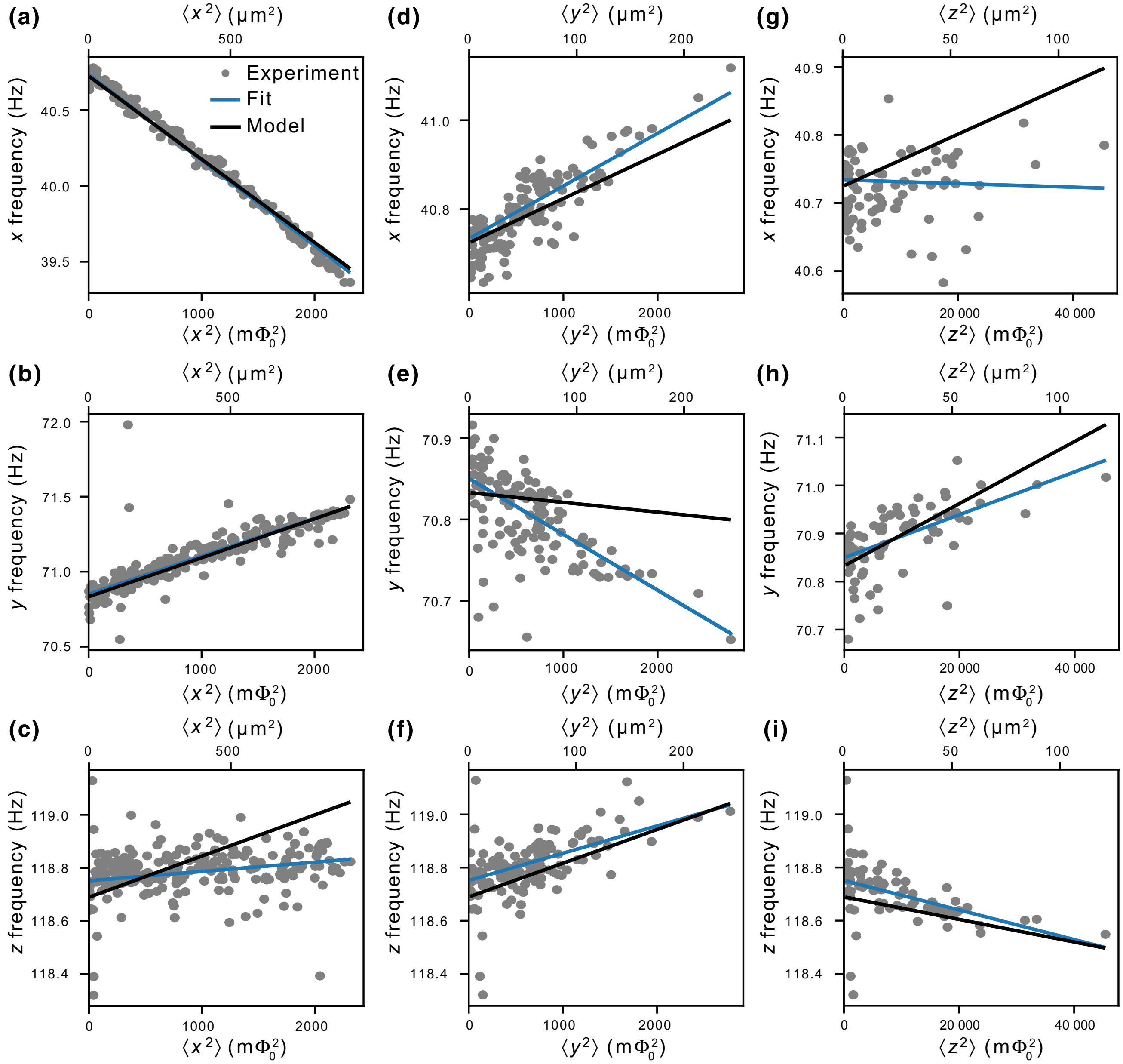

FIG. 12. Frequency pulling. The COM frequencies vary depending on each of the mode amplitudes. Linear fits to the data are represented by blue lines, while the linear relations obtained using the trap anharmonicities extracted from FEM are shown by black lines. In most cases, both lines show a similar slope and capture the behavior reasonably well.

and ω_y on $\langle x^2\rangle$, Figs. 12 and 11 show the dependence of ω_x, ω_y, and ω_z on $\langle x^2\rangle$, $\langle y^2\rangle$, and $\langle z^2\rangle$.

In Fig. 11, the blue-colored straight lines represent linear fits to the data; they are meant as guides to the eye. The model curves are given by Eq. (3) in the main text. We extract estimates of the γ_{ij} values from FEM (details in Appendix A). In Figs. 12(a)–12(i), the x axes are the mean-square displacements in units of m#$_0^2$ and thus the gradients of the nine model lines depend on the three pickup efficiencies η_i [in Figs. 12(a)–(c), the gradients depend on η_x, in Figs. 12(d)–(f) they depend on η_y, and in Figs. 12(g)–(i) they depend on η_z]. We treat the three pickup efficiencies as free parameters and we obtain three estimates for each η_i, from the data in each of the panels. We choose the values that provide the best agreement between the observations and the model. In this way, we use the frequency-pulling data to estimate the pickup efficiencies η_i.

APPENDIX E: FREQUENCY JUMPS

When we levitate a particle, we occasionally observe sudden changes of all the COM frequencies at once. These changes appear to happen at random times. We expect that these frequency jumps are due to reorientation of trapped

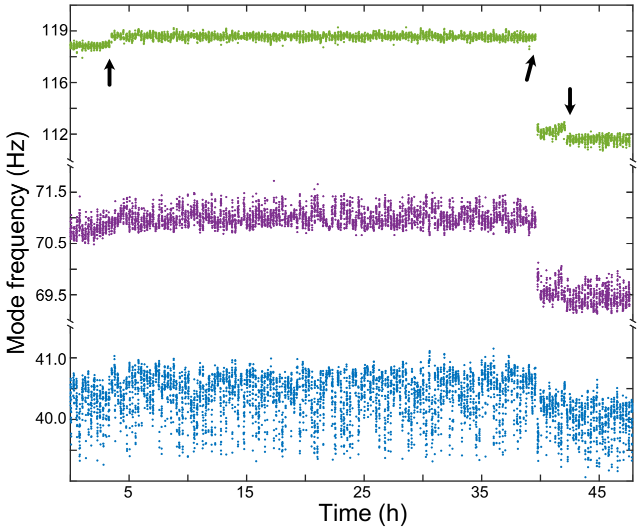

FIG. 13. The COM frequencies measured over 48 h. The arrows indicate times when there are sudden simultaneous jumps of all the COM frequencies.

flux in the particle or due to a change of the amount of the trapped flux in the particle. In Fig. 13, three such frequency jumps are indicated by arrows. Here, the particle has been levitated for two days. The 35-h data set used in Figs. 3 and 4 uses the data between time 4 h and 39 h of this data set.

[1] A. Ashkin and J. M. Dziedzic, Optical levitation in high vacuum, Appl. Phys. Lett. **28**, 333 (1976).

[2] J. Millen, T. S. Monteiro, R. Pettit, and A. N. Vamivakas, Optomechanics with levitated particles, Rep. Prog. Phys. **83**, 026401 (2020).

[3] C. Gonzalez-Ballestero, M. Aspelmeyer, L. Novotny, R. Quidant, and O. Romero-Isart, Levitodynamics: Levitation and control of microscopic objects in vacuum, Science **374**, 3027 (2021).

[4] G. Ranjit, M. Cunningham, K. Casey, and A. A. Geraci, Zeptonewton force sensing with nanospheres in an optical lattice, Phys. Rev. A **93**, 053801 (2016).

[5] J. Prat-Camps, C. Teo, C. C. Rusconi, W. Wieczorek, and O. Romero-Isart, Ultrasensitive Inertial and Force Sensors with Diamagnetically Levitated Magnets, Phys. Rev. Appl. **8**, 034002 (2017).

[6] F. Monteiro, W. Li, G. Afek, C.-l. Li, M. Mossman, and D. C. Moore, Force and acceleration sensing with optically levitated nanogram masses at microkelvin temperatures, Phys. Rev. A **101**, 053835 (2020).

[7] T. Weiss, M. Roda-Llordes, E. Torrontegui, M. Aspelmeyer, and O. Romero-Isart, Large Quantum Delocalization of a Levitated Nanoparticle Using Optimal Control: Applications for Force Sensing and Entangling via Weak Forces, Phys. Rev. Lett. **127**, 023601 (2021).

[8] J. M. Goodkind, The superconducting gravimeter, Rev. Sci. Instrum. **70**, 4131 (1999).

[9] M. V. Moody, H. J. Paik, and E. R. Canavan, Three-axis superconducting gravity gradiometer for sensitive gravity experiments, Rev. Sci. Instrum. **73**, 3957 (2002).

[10] M. T. Johnsson, G. K. Brennen, and J. Twamley, Macroscopic superpositions and gravimetry with quantum magnetomechanics, Sci. Rep. **6**, 37495 (2016).

[11] F. Monteiro, S. Ghosh, A. G. Fine, and D. C. Moore, Optical levitation of 10-ng spheres with nano-g acceleration sensitivity, Phys. Rev. A **96**, 063841 (2017).

[12] C. Timberlake, G. Gasbarri, A. Vinante, A. Setter, and H. Ulbricht, Acceleration sensing with magnetically levitated oscillators above a superconductor, Appl. Phys. Lett. **115**, 224101 (2019).

[13] T. Li, S. Kheifets, D. Medellin, and M. G. Raizen, Measurement of the instantaneous velocity of a Brownian particle, Science **328**, 1673 (2010).

[14] J. Gieseler and J. Millen, Levitated nanoparticles for microscopic thermodynamics—a review, Entropy **20**, 326 (2018).

[15] M. Debiossac, D. Grass, J. J. Alonso, E. Lutz, and N. Kiesel, Thermodynamics of continuous non-Markovian feedback control, Nat. Commun. **11**, 1360 (2020).

[16] K. Dholakia and P. Zemánek, Colloquium: Gripped by light: Optical binding, Rev. Mod. Phys. **82**, 1767 (2010).

[17] W. Lechner, S. J. M. Habraken, N. Kiesel, M. Aspelmeyer, and P. Zoller, Cavity Optomechanics of Levitated Nanodumbbells: Nonequilibrium Phases and Self-Assembly, Phys. Rev. Lett. **110**, 143604 (2013).

[18] S. H. Simpson, L. Chvátal, and P. Zemánek, Synchronization of colloidal rotors through angular optical binding, Phys. Rev. A **93**, 023842 (2016).

[19] J. Yan, X. Yu, Z. V. Han, T. Li, and J. Zhang, On-demand assembly of optically-levitated nanoparticle arrays in vacuum, ArXiv:2207.03641 (2022).

[20] J. Rieser, M. A. Ciampini, H. Rudolph, N. Kiesel, K. Hornberger, B. A. Stickler, M. Aspelmeyer, and U. Delić, Tunable light-induced dipole-dipole interaction between optically levitated nanoparticles, Science **377**, 987 (2022).

[21] T. Delord, L. Nicolas, L. Schwab, and G. Hétet, Electron spin resonance from nv centers in diamonds levitating in an ion trap, New J. Phys. **19**, 033031 (2017).

[22] M. Perdriat, C. Pellet-Mary, P. Huillery, L. Rondin, and G. Hétet, Spin-mechanics with nitrogen-vacancy centers and trapped particles, Micromachines **12**, 651 (2021).

[23] B. A. Stickler, K. Hornberger, and M. S. Kim, Quantum rotations of nanoparticles, Nat. Rev. Phys. **3**, 589 (2021).

[24] C. C. Rusconi, M. Perdriat, G. Hétet, O. Romero-Isart, and B. A. Stickler, Spin-Controlled Quantum Interference of Levitated Nanorotors, Phys. Rev. Lett. **129**, 093605 (2022).

[25] U. Delić, M. Reisenbauer, K. Dare, D. Grass, V. Vuletić, N. Kiesel, and M. Aspelmeyer, Cooling of a levitated nanoparticle to the motional quantum ground state, Science **367**, 892 (2020).

[26] L. Magrini, P. Rosenzweig, C. Bach, A. Deutschmann-Olek, S. G. Hofer, S. Hong, N. Kiesel, A. Kugi, and M. Aspelmeyer, Real-time optimal quantum control of mechanical motion at room temperature, Nature **595**, 373 (2021).

[27] F. Tebbenjohanns, M. L. Mattana, M. Rossi, M. Frimmer, and L. Novotny, Quantum control of a nanoparticle optically levitated in cryogenic free space, Nature **595**, 378 (2021).

[28] A. Ranfagni, K. Børkje, F. Marino, and F. Marin, Two-dimensional quantum motion of a levitated nanosphere, Phys. Rev. Res. **4**, 033051 (2022).

[29] J. Piotrowski, D. Windey, J. Vijayan, C. Gonzalez-Ballestero, A. de los Ríos Sommer, N. Meyer, R. Quidant, O. Romero-Isart, R. Reimann, and L. Novotny, Simultaneous ground-state cooling of two mechanical modes of a levitated nanoparticle, Nat. Phys. 1 (2023).

[30] O. Romero-Isart, A. C. Pflanzer, F. Blaser, R. Kaltenbaek, N. Kiesel, M. Aspelmeyer, and J. I. Cirac, Large Quantum Superpositions and Interference of Massive Nanometer-Sized Objects, Phys. Rev. Lett. **107**, 020405 (2011).

[31] O. Romero-Isart, Quantum superposition of massive objects and collapse models, Phys. Rev. A **84**, 052121 (2011).

[32] P. Z. G. Fonseca, E. B. Aranas, J. Millen, T. S. Monteiro, and P. F. Barker, Nonlinear Dynamics and Strong Cavity Cooling of Levitated Nanoparticles, Phys. Rev. Lett. **117**, 173602 (2016).

[33] D. Goldwater, B. A. Stickler, L. Martinetz, T. E. Northup, K. Hornberger, and J. Millen, Levitated electromechanics: All-electrical cooling of charged nano- and micro-particles, Quantum Sci. Technol. **4**, 024003 (2019).

[34] L. Martinetz, K. Hornberger, J. Millen, M. S. Kim, and B. A. Stickler, Quantum electromechanics with levitated nanoparticles, npj Quantum Inf. **6**, 1 (2020).

[35] L. Dania, D. S. Bykov, M. Knoll, P. Mestres, and T. E. Northup, Optical and electrical feedback cooling of a silica nanoparticle levitated in a Paul trap, Phys. Rev. Res. **3**, 013018 (2021).

[36] F. Moon and P. Chang, *Superconducting Levitation: Applications to Bearings and Magnetic Transportation*, A Wiley Interscience publication (Wiley, 1994).

[37] Y. Takahashi, J. Suzuki, N. Yoneyama, Y. Tokawa, N. Suzuki, F. Matsushima, M. Kumakura, M. Ashida, and Y. Moriwaki, Magnetic trapping of superconducting submicron particles produced by laser ablation in superfluid helium, Appl. Phys. Express **10**, 22701 (2017).

[38] A. Vinante, P. Falferi, G. Gasbarri, A. Setter, C. Timberlake, and H. Ulbricht, Ultralow Mechanical Damping with Meissner-Levitated Ferromagnetic Microparticles, Phys. Rev. Appl. **13**, 064027 (2020).

[39] D. Zheng, Y. Leng, X. Kong, R. Li, Z. Wang, X. Luo, J. Zhao, C.-K. Duan, P. Huang, J. Du, M. Carlesso, and A. Bassi, Room temperature test of the continuous spontaneous localization model using a levitated micro-oscillator, Phys. Rev. Res. **2**, 013057 (2020).

[40] Y. Leng, R. Li, X. Kong, H. Xie, D. Zheng, P. Yin, F. Xiong, T. Wu, C.-K. Duan, and Y. Du, *et al.*, Mechanical Dissipation below 1 μHz with a Cryogenic Diamagnetic Levitated Micro-Oscillator, Phys. Rev. Appl. **15**, 024061 (2021).

[41] C. D. Brown, Y. Wang, M. Namazi, G. I. Harris, M. T. Uysal, and J. G. E. Harris, Superfluid helium drops levitated in high vacuum, ArXiv:2109.05618 (2021).

[42] M. Arrayás, J. L. Trueba, C. Uriarte, and D. E. Zmeev, Design of a system for controlling a levitating sphere in superfluid ^{3}He at extremely low temperatures, Sci. Rep. **11**, 1 (2021).

[43] J. Hofer, G. Higgins, H. Huebl, O. F. Kieler, R. Kleiner, D. Koelle, P. Schmidt, J. A. Slater, M. Trupke, K. Uhl, T. Weimann, W. Wieczorek, F. Wulschner, and M. Aspelmeyer, High-Q magnetic levitation and control of superconducting microspheres at millikelvin temperatures, ArXiv:2211.06289 (2022).

[44] M. G. Latorre, A. Paradkar, D. Hambraeus, G. Higgins, and W. Wieczorek, A chip-based superconducting magnetic trap for levitating superconducting microparticles, IEEE Trans. Appl. Supercond. **32**, 1 (2022).

[45] M. G. Latorre, J. Hofer, M. Rudolph, and W. Wieczorek, Chip-based superconducting traps for levitation of micrometer-sized particles in the Meissner state, Supercond. Sci. Technol. **33**, 105002 (2020).

[46] C. Navau, S. Minniberger, M. Trupke, and A. Sanchez, Levitation of superconducting microrings for quantum magnetomechanics, Phys. Rev. B **103**, 174436 (2021).

[47] O. Romero-Isart, L. Clemente, C. Navau, A. Sanchez, and J. I. Cirac, Quantum Magnetomechanics with Levitating Superconducting Microspheres, Phys. Rev. Lett. **109**, 147205 (2012).

[48] M. Cirio, G. K. Brennen, and J. Twamley, Quantum Magnetomechanics: Ultrahigh-Q-Levitated Mechanical Oscillators, Phys. Rev. Lett. **109**, 147206 (2012).

[49] H. Pino, J. Prat-Camps, K. Sinha, B. P. Venkatesh, and O. Romero-Isart, On-chip quantum interference of a superconducting microsphere, Quantum Sci. Technol. **3**, 025001 (2018).

[50] D. F. Jackson Kimball, A. O. Sushkov, and D. Budker, Precessing Ferromagnetic Needle Magnetometer, Phys. Rev. Lett. **116**, 190801 (2016).

[51] M. Niemetz, W. Schoepe, J. T. Simola, and J. T. Tuoriniemi, The oscillating magnetic microsphere: A tool for investigating vorticity in superconductors and superfluids, Phys. B: Condens. Matter **280**, 559 (2000).

[52] T. Wang, S. Lourette, S. R. O'Kelley, M. Kayci, Y. B. Band, D. F. J. Kimball, A. O. Sushkov, and D. Budker, Dynamics of a Ferromagnetic Particle Levitated over a Superconductor, Phys. Rev. Appl. **11**, 044041 (2019).

[53] J. Gieseler, A. Kabcenell, E. Rosenfeld, J. D. Schaefer, A. Safira, M. J. A. Schuetz, C. Gonzalez-Ballestero, C. C. Rusconi, O. Romero-Isart, and M. D. Lukin, Single-Spin Magnetomechanics with Levitated Micromagnets, Phys. Rev. Lett. **124**, 163604 (2020).

[54] B. R. Slezak, C. W. Lewandowski, J.-F. Hsu, and B. D'Urso, Cooling the motion of a silica microsphere in a magneto-gravitational trap in ultra-high vacuum, New J. Phys. **20**, 063028 (2018).

[55] B. van Waarde, Ph.D. thesis, Universiteit Leiden, The Netherlands (2016).

[56] B. van Waarde, O. Benningshof, and T. Oosterkamp, A magnetic persistent current switch at millikelvin temperatures, Cryogenics **78**, 74 (2016).

[57] J. F. Hsu, P. Ji, C. W. Lewandowski, and B. D'Urso, Cooling the motion of diamond nanocrystals in a magneto-gravitational trap in high vacuum, Sci. Rep. **6**, 1 (2016).

[58] J. D. Weinstein and K. G. Libbrecht, Microscopic magnetic traps for neutral atoms, Phys. Rev. A **52**, 4004 (1995).

[59] J. Reichel, W. Hänsel, and T. W. Hänsch, Atomic Micromanipulation with Magnetic Surface Traps, Phys. Rev. Lett. **83**, 3398 (1999).

[60] I. C. Rodrigues, D. Bothner, and G. A. Steele, Coupling microwave photons to a mechanical resonator using quantum interference, Nat. Commun. **10**, 1 (2019).

[61] D. Zoepfl, M. L. Juan, C. M. F. Schneider, and G. Kirchmair, Single-Photon Cooling in Microwave Magnetomechanics, Phys. Rev. Lett. **125**, 023601 (2020).

[62] P. Schmidt, M. T. Amawi, S. Pogorzalek, F. Deppe, A. Marx, R. Gross, and H. Huebl, Sideband-resolved resonator electromechanics based on a nonlinear Josephson inductance probed on the single-photon level, Commun. Phys. **3**, 1 (2020).

[63] T. Bera, S. Majumder, S. K. Sahu, and V. Singh, Large flux-mediated coupling in hybrid electromechanical system with a transmon qubit, Commun. Phys. **4**, 1 (2021).

[64] T. Luschmann, P. Schmidt, F. Deppe, A. Marx, A. Sanchez, R. Gross, and H. Huebl, Mechanical frequency control in inductively coupled electromechanical systems, Sci. Rep. **12**, 1 (2022).

[65] D. Zoepfl, M. L. Juan, N. Diaz-Naufal, C. M. F. Schneider, L. F. Deeg, A. Sharafiev, A. Metelmann, and G. Kirchmair, Kerr Enhanced Backaction Cooling in Magnetomechanics, Phys. Rev. Lett. **130**, 033601 (2023).

[66] J. Gieseler, L. Novotny, and R. Quidant, Thermal nonlinearities in a nanomechanical oscillator, Nat. Phys. **9**, 806 (2013).

[67] J. Gieseler, M. Spasenovic, L. Novotny, and R. Quidant, Nonlinear Mode Coupling and Synchronization of a Vacuum-Trapped Nanoparticle, Phys. Rev. Lett. **112**, 103603 (2014).

[68] A. Setter, J. Vovrosh, and H. Ulbricht, Characterization of non-linearities through mechanical squeezing in levitated optomechanics, Appl. Phys. Lett. **115**, 153106 (2019).

[69] Y. Zheng, L.-M. Zhou, Y. Dong, C.-W. Qiu, X.-D. Chen, G.-C. Guo, and F.-W. Sun, Robust Optical-Levitation-Based Metrology of Nanoparticle's Position and Mass, Phys. Rev. Lett. **124**, 223603 (2020).

[70] J. Flajšmanová, M. Šiler, P. Jedlička, F. Hrubý, O. Brzobohatý, R. Filip, and P. Zemánek, Using the transient trajectories of an optically levitated nanoparticle to characterize a stochastic Duffing oscillator, Sci. Rep. **10**, 1 (2020).

[71] R. Maisonobe, J. Billard, M. D. Jesus, A. Juillard, D. Misiak, E. Olivieri, S. Sayah, and L. Vagneron, Vibration decoupling system for massive bolometers in dry cryostats, J. Instrum. **13**, T08009 (2018).

[72] M. D. Wit, G. Welker, K. Heeck, F. M. Buters, H. J. Eerkens, G. Koning, H. V. der Meer, D. Bouwmeester, and T. H. Oosterkamp, Vibration isolation with high thermal conductance for a cryogen-free dilution refrigerator, Rev. Sci. Instrum. **90**, 015112 (2019).

[73] M. Rossi, D. Mason, J. Chen, Y. Tsaturyan, and A. Schliesser, Measurement-based quantum control of mechanical motion, Nature **563**, 53 (2018).

[74] J. Hofer and M. Aspelmeyer, Analytic solutions to the Maxwell-London equations and levitation force for a superconducting sphere in a quadrupole field, Phys. Scr. **94**, 125508 (2019).

[75] A. Bachtold, J. Moser, and M. I. Dykman, Mesoscopic physics of nanomechanical systems, Rev. Mod. Phys. **94**, 045005 (2022).

[76] M. Gutierrez Latorre, G. Higgins, A. Paradkar, T. Bauch, and W. Wieczorek, Data and code for the article "Superconducting microsphere magnetically levitated in an anharmonic potential," https://doi.org/10.5281/zenodo.7304534.

[77] D. Drung, C. Abmann, J. Beyer, A. Kirste, M. Peters, F. Ruede, and T. Schurig, Highly sensitive and easy-to-use squid sensors, IEEE Trans. Appl. Supercond. **17**, 699 (2007).

Correction: The omission of a data availability statement and the corresponding reference has been rectified.

Second Correction: The prior Correction to insert a data availability statement and corresponding reference was implemented incorrectly by the production staff and has now been rectified (the source information appearing in Refs. [76] and [77] has been interchanged to align with the citations in the paper).